An Analytical Solution of the Effective-Buoyancy Equation

ROBERT DAVIES-JONES[a]

[a] *NOAA/National Severe Storms Laboratory, Norman, Oklahoma*

ABSTRACT: The effective buoyancy per unit volume is the statically forced part of the local nonhydrostatic upward pressure-gradient force. It is important because it does not depend on the basic-state density defined with the anelastic approximation. Herein, an analytical solution is obtained for the effective buoyancy associated with an axisymmetric column of less dense air. In special cases where the radial profiles of density are step functions, the analytical solutions replicate qualitatively several features in a recently published numerical solution as follows. The effective buoyancy is positive within the column of lighter air and negative outside. It increases from the axis to the inner edge of the column, then jumps discontinuously to a negative value and thereafter increases until it reaches zero at radial infinity. As the column radius increases, the effective buoyancy on the axis decreases and the change in effective buoyancy between the axis and the inner edge increases, but the jump magnitude is unaltered. For continuous radial density distributions that resemble step functions, the solutions are similar except the cusps are rounded off and the jumps become smooth transition zones.

SIGNIFICANCE STATEMENT: In atmospheric convection, vertical accelerations are due to buoyancy forces and vertical perturbation pressure-gradient forces. Separately, these forces depend on the choice of a basic state. To avoid the ambiguity of an arbitrary reference atmosphere defining which parcels are buoyant, we define an effective-buoyancy force per unit volume that is independent of any basic state. It is the part of the vertical nonhydrostatic pressure-gradient force that depends solely on horizontal density variations. The remaining part of the vertical force is dynamical in origin; it depends only on inertial forces. An analytical solution demonstrates that, for an axisymmetric column of lighter air, effective buoyancy is greatest just inside the column edge and is most negative just outside the edge.

1. Introduction

Davies-Jones (2003, hereafter DJ03) conceived the idea of effective buoyancy, which has the important property of being independent of an arbitrary base state. It is an important diagnostic for thermals (Tarshish et al. 2018), cumulus parameterizations in climate models (Pauluis and Garner 2006), tropical cyclones (Smith and Montgomery 2022, hereafter SM22), and density currents (Jeevanjee and Romps 2015, hereafter JR15). It is equal to the "buoyancy forcing of vertical acceleration," which had been used earlier in diagnostics of supercell simulations (e.g., Rotunno and Klemp 1982; Emanuel 1994, p. 385) without explicit recognition that it is an absolute quantity. Buoyancy forcing of vertical acceleration is comprised of separate terms that depend on perturbations from an arbitrary base state. It is the sum of conventional buoyancy (which depends on perturbation density) and a vertical perturbation pressure-gradient force (VPPGF). Thus conventional buoyancy and VPPGF, both of which are used for physical interpretation, are relative quantities (DJ03; Doswell and Markowski 2004). They individually vary with the arbitrary choice of reference density and pressure profiles although their sum does not. In contrast to buoyancy forcing of

vertical acceleration, effective buoyancy eliminates the need for a base state.

Effective buoyancy per unit volume is defined as follows. Pressure, p, may be split into local hydrostatic pressure, p_h, and local nonhydrostatic pressure $p_{nh} = p - p_h$. The nonhydrostatic vertical pressure-gradient force can then be divided into a static part, $-\partial p_\beta/\partial z$, and a dynamic part, $-\partial p_\gamma/\partial z$, according to the forcing terms in the Poisson equation for nonhydrostatic vertical pressure-gradient force. The static part, $\beta \equiv -\partial p_\beta/\partial z$, is the effective buoyancy (DJ03).

The anelastic approximation, which eliminates sound waves, is used in the derivations of effective buoyancy. Contra to Einstein's equivalence principle, the anelastic approximation uses a different density for inertia [the environmental or base-state density at the parcel height $\rho_0(z)$] than for gravity (the parcel's actual density ρ). The inertial density is, in general, an arbitrary function of just height, z.

DJ03 showed that the effective buoyancy force per unit volume (β) is independent of the horizontal location of the density profile (i.e., the "environmental sounding") and derived its governing equation. Due to the inertial mass being marginally different from the gravitational mass, effective buoyancy per unit mass does depend *slightly* on the reference density as indicated in section 2.

Pauluis and Garner (2006) implicitly used a control-volume flux approach to eliminate the radial dependency from the Poisson equation governing effective buoyancy. The control volumes are thin horizontal slices of a column of air that is less dense than its surroundings. They solved the resulting

Davies-Jones: Emeritus

Corresponding author: Robert Davies-Jones, bobdj1066@yahoo.com

equation as a function of height using a Green's function method. They found that the effective buoyancy is much smaller for a wide parcel than for a narrow one.

Jeevanjee and Romps (2016, hereafter JR16) considered the effective buoyancies of a "free" cylindrical-shaped fluid density anomaly in an infinite domain and of one based on the ground in a semi-infinite domain. They assumed that the density deficit within the cylinder is constant. JR16 were able to obtain solutions only for the effective buoyancy along the cylinder axis. They found that the axial effective buoyancy was always smaller than the Archimedean buoyancy and that it decreased with decreasing height-to-width (aspect) ratio of the cylinder. [The Archimedean buoyancy force is defined as the upward force exerted upon a parcel of fluid in a gravitational field by virtue of the density difference between the parcel and that of the surrounding fluid (Glickman 2000; Doswell and Markowski 2004).]

As easily predicted by the method of images (DJ03), the effective buoyancy of the surface-based cylinder is less than for the free cylinder. Tarshish et al. (2018) showed that the effective buoyancy of a thermal also decreases with aspect ratio. This result is anticipated by the linear theory of thermal convection (Saltzman 1962). Wide flat convective cells are less efficient at transporting heat than narrow tall ones because a greater proportion of the potential energy is converted into horizontal kinetic energy rather than vertical kinetic energy. If there were no dissipation, the most unstable convective cells would be infinitely narrow. In a real fluid, energy dissipation is largest for narrow cells so the most unstable cells have finite width. In cumulus convection, the situation is similar. Because entrainment-driven dilution depends inversely on radius, the narrowest convective elements quickly lose their buoyancy through mixing with ambient air. On the other hand, very wide updrafts have small effective buoyancies. Hence the strongest convective updrafts have intermediate widths (Morrison 2017).

SM22 investigated the effective buoyancy per unit mass of a finite column of less dense air. The density deficit within the column varies sinusoidally with height and is constant in the radial direction. The radial density profile is thus a step function. They found that the effective buoyancy is always positive within the column. Even though the buoyancy itself is horizontally uniform across the column, the effective buoyancy is not. As the width of the buoyancy column increases, the effective buoyancy becomes smaller in the center of the column, and the maximum effective buoyancy becomes located at the inner edge of the column. In the environment, the effective buoyancy is negative with a narrow sheath of strong negative buoyancy at the outer edge of the column. Thus, the largest values of effective buoyancy, both positive and negative, are found just inside and outside the column edge.

The current paper is basically an extension of SM22's work. SM22 presented numerical solutions for the effective buoyancy associated with a two-dimensional slab of less dense fluid. This paper obtains analytical solutions for the effective buoyancy of a cylindrical column of less dense fluid and, in some cases, for continuous radial density profiles. In contrast to SM22's problem, there are no side boundaries and the

buoyant column extends all the way from the ground to the top boundary. Analytical solutions are important because they apply for all parametric values, not just a select few. The analytical solutions based on DJ03 theory successfully replicate the qualitative features of SM22's numerical solutions.

The paper is organized as follows. Section 2 summarizes the DJ03 analysis for reference in later sections. An analytical solution for the effective buoyancy of a density field with a sinusoidal vertical profile is obtained in section 3. This solution is tailored for a column of less dense air in section 4. Section 5 presents the effective-buoyancy solution for a radial density profile that is continuous instead of a step function.

2. The DJ03 theory revisited

For later reference we derive the theory of effective buoyancy without introducing an unnecessary base state and perturbations. The anelastic Euler equation of motion and the continuity equation are

$$\rho_0 \frac{\partial \mathbf{u}}{\partial t} + \rho_0 \mathbf{u} \cdot \boldsymbol{\nabla} \mathbf{u} = -\boldsymbol{\nabla} p - g\rho \mathbf{k}, \qquad (1)$$

$$\boldsymbol{\nabla} \cdot (\rho_0 \mathbf{u}) = 0, \qquad (2)$$

where ρ is the gravitational density, $\rho_0(z)$ is the inertial density, z is height above ground, $\mathbf{u}$ is the wind vector, and $\mathbf{k}$ is the unit upward vector. By taking the divergence of (1) and using (2), we obtain the diagnostic pressure equation:

$$-\boldsymbol{\nabla}^2 p = g \frac{\partial \rho}{\partial z} + \boldsymbol{\nabla} \cdot (\rho_0 \mathbf{u} \cdot \boldsymbol{\nabla} \mathbf{u}). \qquad (3)$$

In DJ03 the pressure, p, is split into a local hydrostatic component p_h for which

$$\frac{\partial p_h}{\partial z} = -g\rho \qquad (4)$$

and a nonhydrostatic component $p_{\mathrm{nh}} = p - p_h$. Inserting this pressure decomposition in (3) and introducing (4) produces

$$-\boldsymbol{\nabla}^2 p_{\mathrm{nh}} = \boldsymbol{\nabla}^2 p_h + g\frac{\partial \rho}{\partial z} + \boldsymbol{\nabla} \cdot (\rho_0 \mathbf{u} \cdot \boldsymbol{\nabla} \mathbf{u}) = \nabla_H^2 p_h + \boldsymbol{\nabla} \cdot (\rho_0 \mathbf{u} \cdot \boldsymbol{\nabla} \mathbf{u}). \qquad (5)$$

Differentiating (5) with respect to z and using (4) again gives

$$\boldsymbol{\nabla}^2\left(-\frac{\partial p_{\mathrm{nh}}}{\partial z}\right) = -g\nabla_H^2\rho + \frac{\partial}{\partial z}\boldsymbol{\nabla} \cdot (\rho_0 \mathbf{u} \cdot \boldsymbol{\nabla} \mathbf{u}). \qquad (6)$$

By inserting the pressure decomposition into the vertical component of (1) and using (4), we obtain

$$\rho_0 \frac{\partial w}{\partial t} + \rho_0 \mathbf{u} \cdot \boldsymbol{\nabla} w = -\frac{\partial p_{\mathrm{nh}}}{\partial z}, \qquad (7)$$

where w is the vertical velocity. At the ground ($z = 0$) and at a solid top boundary ($z = h$), $w = 0$ so $\partial p_{\mathrm{nh}}/\partial z = 0$ there. Given the current density field, the current wind field and its tendency, we can solve the Poisson Eq. (6) subject to

$\partial p_{\text{nh}}/\partial z = 0$ at horizontal boundaries. In this formulation, the dependent variable is the vertical force, $-\partial p_{\text{nh}}/\partial z$, and the boundary conditions (BCs) are Dirichlet ones for this variable. The forcing function consists of a static forcing and a dynamic forcing [the first and second terms on the right of (6), respectively]. After decomposing the vertical force per unit volume $-\partial p_{\text{nh}}/\partial z$ into its static part β and its dynamic part γ, the vertical equation of motion becomes

$$\rho_0 \frac{dw}{dt} = \beta + \gamma. \tag{8}$$

Since the boundary-value problem is linear, we can split it as follows:

$$-\boldsymbol{\nabla}^2\beta = g\boldsymbol{\nabla}_H^2\rho, \quad \beta = 0 \quad \text{at } z = 0, h, \tag{9}$$

$$\boldsymbol{\nabla}^2\gamma = \frac{\partial}{\partial z}\boldsymbol{\nabla}\cdot(\rho_0\mathbf{u}\cdot\boldsymbol{\nabla}\mathbf{u}), \quad \gamma = 0 \quad \text{at } z = 0, h. \tag{10}$$

The effective-buoyancy equation is the one in (9). The forcing function for effective buoyancy is $g\boldsymbol{\nabla}_H^2\rho$. Adding (9) and (10) recovers (6) and the BCs on $\partial p_{\text{nh}}/\partial z$. Clearly β is the part of the vertical force that depends on horizontal variations in gravitational mass and is independent of inertial mass, whereas γ depends on inertial forces. If $\partial p_{\text{nh}}/\partial z \neq 0$ on any part of the domain boundaries, then there is also a third part, ε, namely, the solution of the Laplace equation $\boldsymbol{\nabla}^2\varepsilon = 0$ subject to the BCs.

The effective buoyancy is an absolute quantity because the forcing function in (9) is independent of the reference density. Hence there is no need to complicate its derivation by introducing a reference density and deviations from it.

From (8) the parcel vertical acceleration due to β is β/ρ_0, which equals $[1 + (\rho - \rho_0)/\rho_0]\beta/\rho$ for small $(\rho - \rho_0)/\rho_0$. Thus the effective buoyancy per unit mass, β/ρ_0, does depend slightly on the base state. However, the radial variations of effective buoyancy per unit mass and effective buoyancy per unit volume will be similar because ρ_0 is a function of height only.

Davies-Jones (2002) considered the effects of horizontal variations in the dynamical nonhydrostatic vertical pressure-gradient force (i.e., γ) on the tilting and propagation of supercell updrafts. Among other results he found that wider updrafts are less prone to bending over in strong vertical shear. This paper only concerns β, the effective buoyancy.

3. Some solutions for effective buoyancy

For simple geometries and specified density distributions, we can obtain solutions of the boundary-value problem (9) for β via separation of variables. Here we assume axisymmetric density fields of the form

$$\rho(x, z) = \Sigma(z) + \sigma(x)\sin(\pi z/h), \tag{11}$$

where r is the radial coordinate and $x \equiv \pi r/h$ is a *scaled radial coordinate* (*not* a Cartesian coordinate). This decomposition is somewhat arbitrary because

$$\rho(x, z) = \hat{\Sigma}(z) + \hat{\sigma}(x)\sin(\pi z/h),$$

$$\text{where } \hat{\Sigma}(z) \equiv \Sigma(z) + \sigma_0\sin(\pi z/h), \tag{12}$$

$$\hat{\sigma}(x) \equiv \sigma(x) - \sigma_0$$

has the same mathematical form as (11) for any constant σ_0. Inserting (11) into (9) yields

$$\boldsymbol{\nabla}_H^2\beta + \frac{\partial^2\beta}{\partial z^2} = -g\boldsymbol{\nabla}_H^2\sigma(x)\sin\frac{\pi z}{h}, \quad \beta = 0 \quad \text{at } z = 0, h, \tag{13}$$

so the governing equation for β is independent of $\Sigma(z)$ and σ_0. At the axis of very narrow columns of less dense air, $|\boldsymbol{\nabla}_H^2\beta| \gg |\partial^2\beta/\partial z^2|$, and the solution of (13) there is approximately

$$\beta(0, z) \approx g[\sigma(\infty) - \sigma(0)]\sin(\pi z/h) \tag{14}$$

if we assume that $\beta(\infty, z) = 0$. Thus the difference between β and buoyancy per unit volume vanishes at the axis in the limit of an infinitely narrow column. In the opposite extreme of a very wide column with a flat density minimum, $|\boldsymbol{\nabla}_H^2\beta| \ll |\partial^2\beta/\partial z^2|$ at the axis and

$$\beta(0, z) \approx \frac{gh^2}{\pi^2}(\boldsymbol{\nabla}_H^2\sigma)(0)\sin(\pi z/h). \tag{15}$$

In this case, the effective buoyancy at the central axis tends to 0^+ as the column width tends to ∞.

To separate variables, we look for solutions of (13) that have the form

$$\beta(x, z) = E(x)\sin(\pi z/h). \tag{16}$$

In terms of x, we may write the operator $\boldsymbol{\nabla}_H^2$ as

$$\boldsymbol{\nabla}_H^2 = \frac{\pi^2}{h^2}\frac{1}{x}\frac{d}{dx}\left(x\frac{d}{dx}\right). \tag{17}$$

Introducing (16) and (17) into (13) yields

$$\frac{d}{dx}\left[x\frac{d(E + g\sigma)}{dx}\right] - (E + g\sigma)x = -g\sigma x. \tag{18}$$

By adding the constant $g\sigma(\infty)$, to both sides of (18) and defining $y(x) \equiv E(x) + g\sigma(x) - g\sigma(\infty)$ as the dependent variable, we obtain

$$L(y) \equiv \frac{d}{dx}\left(x\frac{dy}{dx}\right) - xy = -g[\sigma(x) - \sigma(\infty)]x. \tag{19}$$

The homogeneous version of (19), $L(y) = 0$, is a modified Bessel equation with the general solution

$$y(x) = c_1 I_0(x) + c_2 K_0(x), \tag{20}$$

where I_n and K_n are modified Bessel functions of integer order n of the first and second kind, respectively, and c_1 and c_2 are constants. Relevant identities involving the modified Bessel functions are listed in the appendix for reference.

We obtain the solution of the inhomogeneous Eq. (19) by the Green's function method (Hildebrand 1965, 228–231). The basic method depends on homogeneous BCs. For our problem we choose

$$dy/dx = 0 \quad \text{at } x = 0, \quad y = 0 \quad \text{at } x = \infty \qquad (21)$$

based on axisymmetry at the axis and $E = 0$ at radial infinity. The solution is of the form

$$y(x) = \int_{s=0}^{\infty} G(x,s)g[\sigma(s) - \sigma(\infty)]s\,ds, \qquad (22)$$

where the Green's function

$$G(x,s) \equiv \begin{cases} G_1(x,s) & \text{for } x < s \\ G_2(x,s) & \text{for } x > s. \end{cases} \qquad (23)$$

For (23) to be a solution of the boundary-value problem (19) and (21), the following conditions must hold (Hildebrand 1965, p. 229):

1) $L(G_1) = 0$ when $x < s$ and $L(G_2) = 0$ when $x > s$.
2) G_1 and G_2 must obey the given BCs, viz $dG_1/dx = 0$ at $x = 0$, $G_2 = 0$ at $x = \infty$.
3) G is continuous so $G_1 = G_2$ at $x = s$.
4) $dG_2/dx - dG_1/dx = -1/x$ at $x = s$.

Suppose that

$$\begin{aligned} G(x,s) = G_1(x,s) = I_0(x)K_0(s) & \quad \text{for } x < s, \\ G(x,s) = G_2(x,s) = K_0(x)I_0(s) & \quad \text{for } x > s. \end{aligned} \qquad (24)$$

The first and third conditions are met because I_0 and K_0 are solutions of $L(y) = 0$ [see (20)] and G is obviously continuous. By (A3), (A4), and (24),

$$\begin{aligned} \frac{\partial G_1}{\partial x} = I_1(x)K_0(s) & \quad \text{for } x < s, \\ \frac{\partial G_2}{\partial x} = -K_1(x)I_0(s) & \quad \text{for } x > s. \end{aligned} \qquad (25)$$

Since $I_1(0) = 0$ and $K_1(\infty) = 0$, the second condition is met. At $x = s$,

$$\frac{dG_2}{dx} - \frac{dG_1}{dx} = -I_0(x)K_1(x) - I_1(x)K_0(x). \qquad (26)$$

According to (A18) the right side is the Wronskian, $W(x)$, of $I_0(x)$ and $K_0(x)$, which is equal to $-1/x$ by (A19) so the fourth condition is fulfilled. Therefore by introduction of (24) into (22), the solution for the effective buoyancy radial profile is

$$E(x) = -g[\sigma(x) - \sigma(\infty)] + K_0(x)\int_{s=0}^{x} sI_0(s)g[\sigma(s) - \sigma(\infty)]ds$$

$$+ I_0(x)\int_{s=x}^{\infty} sK_0(s)\,g[\sigma(s) - \sigma(\infty)]ds. \qquad (27)$$

Ostensibly, (27) indicates that $E(x)$ depends on $\sigma(\infty)$. However, this is not the case because we can eliminate $\sigma(\infty)$ by adding $g\sigma(\infty)$ times (A21) to (27). This yields

$$E(x) = -g\sigma(x) + K_0(x)\int_{s=0}^{x} sI_0(s)g\sigma(s)ds$$

$$+ I_0(x)\int_{s=x}^{\infty} sK_0(s)g\sigma(s)ds. \qquad (28)$$

To simplify explanations later on, we subtract $g\sigma(0)$ times (A21) from (28) and divide the result by $g[\sigma(\infty) - \sigma(0)]$, which gives us

$$E_*(x) = -\sigma_*(x) + K_0(x)\int_{s=0}^{x} sI_0(s)\sigma_*(s)ds$$

$$+ I_0(x)\int_{s=x}^{\infty} sK_0(s)\sigma_*(s)ds, \qquad (29)$$

where $\sigma_*(x) \equiv [\sigma(x) - \sigma(0)]/[\sigma(\infty) - \sigma(0)]$ is a nondimensional deviation of density from its axial value at the same level, and $E_* \equiv E/g[\sigma(\infty) - \sigma(0)]$ is the nondimensional effective buoyancy radial profile (NEBRP). By (16), (24), and (29), the nondimensional effective buoyancy (NEB) $\beta_* \equiv \beta/g[\sigma(\infty) - \sigma(0)]$ is given by

$$\begin{aligned} \beta_*(x,z) &= E_*(x)\sin(\pi z/h) \\ &= \left[-\sigma_*(x) + \int_{s=0}^{\infty} G(x,s)\sigma_*(s)s\,ds\right]\sin(\pi z/h). \end{aligned} \qquad (30)$$

In dimensional terms,

$$\beta(x,z) = -g\sigma(x)\sin(\pi z/h) + \sin(\pi z/h)\int_{s=0}^{\infty} G(x,s)g\sigma(s)s\,ds. \qquad (31)$$

Hildebrand (1965, p. 242) provides the physical interpretation of the Green's function, which is customized to solution (30) as follows. Since $\sin(\pi z/h)$ is a common factor in (30), we may restrict our attention to the relationship between E_* and σ_* at one level. The differential effect on the variable $E_* + \sigma_*$ at a field point x due to a cause $\sigma_*(s)$ distributed over the infinitesimally thin annulus of influence points defined by inner and outer radii s and $s + ds$ is $G(x,s)\sigma_*(s)s\,ds$. Hence the Green's function $G(x,s)$ represents the effect on the dependent variable at the field point x due to a unit cause concentrated at the influence circle s. The solution (30) is the sum of the effects at x induced by the causes from all the influence circles, s.

4. Solution for a step function radial density profile

In this section, we suppose that the nondimensional excess-density radial profile is a step function of the form

$$\sigma_*(x) = H(x - X), \qquad (32)$$

where the Heaviside step function

$$H(x - X) \equiv \begin{cases} 0 & \text{for } x < X \\ 0.5 & \text{for } x = X; \\ 1 & \text{for } x > X \end{cases} \qquad (33)$$

$X \equiv \pi R/h$ where R is the radius of the column of less dense air and h/R is an aspect ratio. Note that $r = R$ where $x = X$ and the jump in σ_* at the column edge is 1.
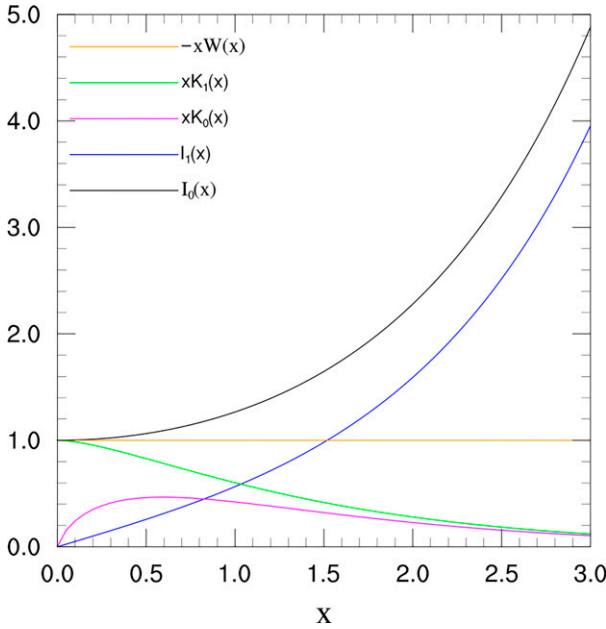
FIG. 1. Graphs of the Bessel-related functions: $I_0(x)$, $I_1(x)$, $xK_0(x)$, $xK_1(x)$, and $-xW(x)$.

FIG. 2. Nondimensional effective-buoyancy radial profile E_* (NEBRP) as a function of r/h for columns of nondimensional radii $R/h = 0.1$, 0.3 and 0.5. As $R/h \rightarrow 0$ and the column becomes very thin, $E_* \rightarrow 1$ inside the column and $E_* \rightarrow 0$ outside it.

Inserting (32) and (33) into (30) yields

$$E_*(x) = -H(x-X) + \int_{s=0}^{\infty} G(x,s)H(s-X)s\,ds$$

$$= \begin{cases} \int_{s=X}^{\infty} G(x,s)s\,ds & \text{for } x < X \\ -1 + \int_{s=X}^{\infty} G(x,s)s\,ds & \text{for } x > X \end{cases}, \quad (34)$$

and then introducing (24) produces

$$E_*(x) = \begin{cases} I_0(x)\int_{s=X}^{\infty} sK_0(s)ds & \text{for } x < X \\ -1 + K_0(x)\int_{s=X}^{x} sI_0(s)ds + I_0(x)\int_{s=x}^{\infty} sK_0(s)ds & \text{for } x > X. \end{cases} \quad (35)$$

With use of (A7), (A8), (A14), and (A20), this simplifies to

$$E_*(x) = \begin{cases} XK_1(X)I_0(x) & \text{for } x < X \\ -XI_1(X)K_0(x) & \text{for } x > X. \end{cases} \quad (36)$$

Thus the NEBRP depends on the functions $I_0(x)$, $I_1(x)$, $xK_0(x)$, and $xK_1(x)$, which are graphed in Fig. 1. We evaluated these functions using Press et al.'s (1992, 230–233) code for the modified Bessel functions $I_0(x)$, $I_1(x)$, $K_0(x)$, and $K_1(x)$. This code uses formulas from Abramowitz and Stegun (1964). It was converted to Fortran 90 and slightly modified to provide $xK_0(x)$ and $xK_1(x)$ for all $x \geq 0$ instead of $K_0(x)$ and $K_1(x)$ for $x > 0$. Because $K_0(x)$ and $K_1(x)$ are infinite at $x = 0$, they were not used without the multiplier x.

The NEBRP in (36) varies with the nondimensional radial coordinate r/h ($\equiv x/\pi$) as shown in Fig. 2. The various graphs
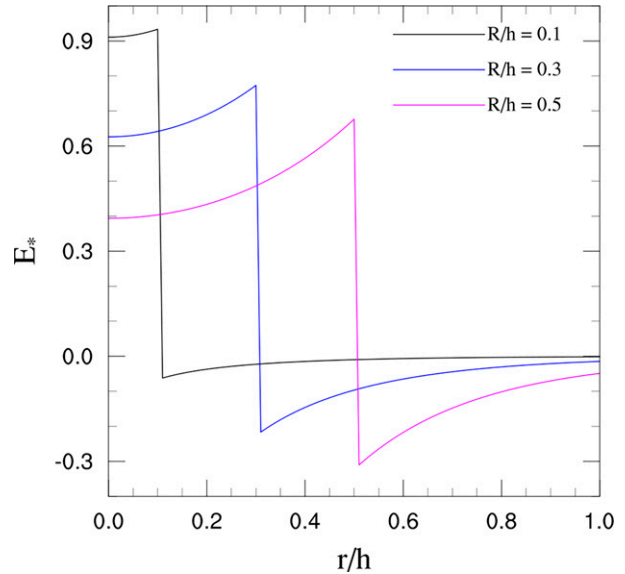
are for different column aspect ratios h/R. NEBRP is positive inside the column and negative outside. It increases from its axial value

$$E_*(0) = XK_1(X) \quad (37)$$

to its maximum value just inside the column edge (SM22; JR15),

$$E_*(X^-) = XI_0(X)K_1(X), \quad (38)$$

jumps to its minimum value

$$E_*(X^+) = -XI_1(X)K_0(X), \quad (39)$$

and then decays to zero at $x = \infty$. At $x = X$, the NEBRP has a discontinuity of magnitude

$$E_*(X^+) - E_*(X^-) = -X[I_1(X)K_0(X) + I_0(X)K_1(X)]$$
$$= XW(X) = -1 \quad (40)$$

from (A20). Similar behavior is evident in SM22's Fig. 4, which is for slab (2D) symmetry instead of axisymmetry. The variations in the analytical solutions with column radius are similar to the variations of SM22's numerical solutions with slab width. Since

$$\sigma_*(X^+) - \sigma_*(X^-) = 1 \quad (41)$$

from (32) and (33), it is evident from (40) that $E_* + \sigma_*$ is continuous at $x = X$. The jump in E_* is equal and opposite to the one in σ_*. Since the jump is always -1 for all aspect ratios and the maximum E_* decreases with R/h, the negative extremum become larger in magnitude with decreasing
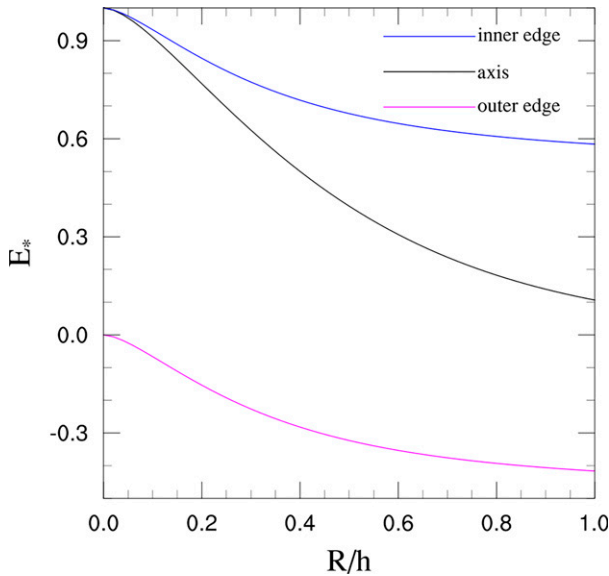
FIG. 3. Nondimensional effective-buoyancy radial profile as a function of nondimensional column radius R/h for three different radial locations, namely, on the axis, just inside the side of the cylinder, and just outside the edge.

aspect ratio. Taking the derivative of (36) and applying (A3) and (A4) yields

$$\frac{dE_*(x)}{dx} = \begin{cases} X K_1(X) I_1(x) & \text{for } x < X \\ X I_1(X) K_1(x) & \text{for } x > X. \end{cases} \quad (42)$$

As evident in Fig. 2, the horizontal gradient of NEBRP is zero at the axis and radial infinity, continuous at the column edge, and nonnegative. In contrast to the above behavior, Tarshish et al. (2018) found that for ellipsoidal density anomalies β is uniform within the anomaly.

Figure 3 shows how the NEBRP on the axis and at the inner and outer sides of the column varies with column radius. From (37), (A12), and (A14), the NEBRP at the axis decreases from 1 to 0.1 to 0 as R/h increases from 0 to 1 to ∞ (see Fig. 3). In JR16, the variation for their surface cylinder case is similar except the NEBRP is 0.25 at $R/h = 1$ (their Fig. 4). In JR16 the presence of a lower boundary reduces the NEBRP by half. Herein, there is also an upper boundary so it is reasonable to expect a further 50%, which would make the present and JR16 values comparable. The maximum NEBRP occurs at the column's inner edge. From (38), (A9), and (A12), it is 1 at $X = 0$ and from (38), (A13), and (A14), it tends to 0.5 as $X \to \infty$. Owing to the negative jump of -1 in NEBRP across the edge, the minimum NEBRP at the outer edge decreases from 0 for $X = 0$ to -0.5 at $X = \infty$.

In agreement with (14), (15), and previous studies (see introduction), the effective buoyancy is slightly less than the buoyancy for very narrow step function columns and for very wide ones it is much less. The effective buoyancy just inside the step function column edge decreases with column
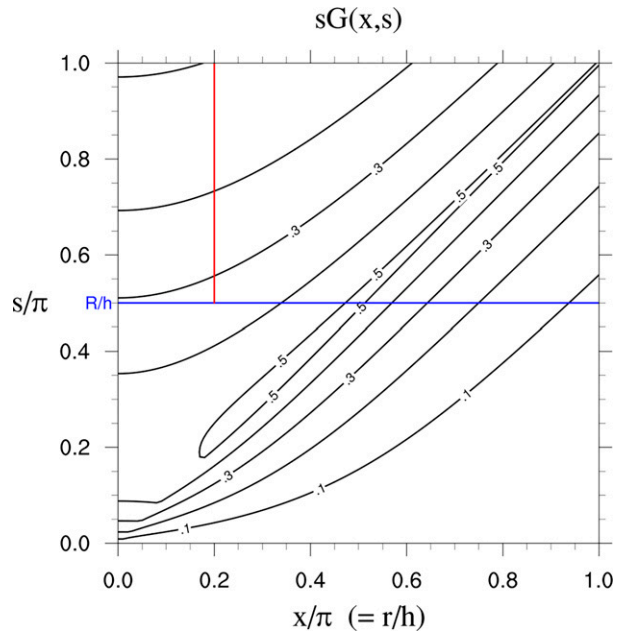

FIG. 4. Contour diagram of $sG(x, s)$, the integrand in (34). The contour interval is 0.1. The blue line $s/\pi = R/h$ represents the lower limit of the integrals in (34) (illustrated here for $R/h = 0.5$). The red line, which extends to infinity, is the path of integration, which is from $s = X$ to $s = \infty$ at fixed x (drawn here for 0.2π).

radius and that just outside is more negative for wider columns, as in SM22.

We now offer some explanation for the effective buoyancy associated with the step function density distribution. Note that we can concentrate just on the physics in the midlevel plane since the effective buoyancy, $\beta_* = E_*(x)\sin(\pi z/h)$, and the part of the density field that affects it, $\sigma_*(x)\sin(\pi z/h)$, at other levels are simply $\sin(\pi z/h)$ multiples of their midlevel counterparts. Contours of $sG(x, s)$, which is the integrand in (34), are plotted in Fig. 4. Since $\sigma_* = 0$ inside the column and $= 1$ outside in this formulation, the density excesses are uniform in strength and are located at influence points that are outside the column. Points inside the column exert no influence. Because there are no negative influences, the integrand is positive definite. The influence region can be partitioned into annuli with inner and outer radii s and $s + \delta s$ with uniform thickness δs. In (34), the factor s appears in the integrand because the number of influence points per annulus increases linearly with s (if the problem were discretized on a uniform grid). The integrations in (34) at a fixed x, say $x = 0.2$, are performed along the red line, which extends from $s = X$, represented by the blue line, to infinity.

We can visualize how the integral in (34) varies with x by sliding the red line to different x. Clearly the integral increases with x. Thus the effective buoyancy inside the column increases from the axis to the inner edge, and would keep on increasing but for the jump of -1 at the edge [see (34)]. Incorporating the jump produces the NEBRPs shown in Fig. 2.
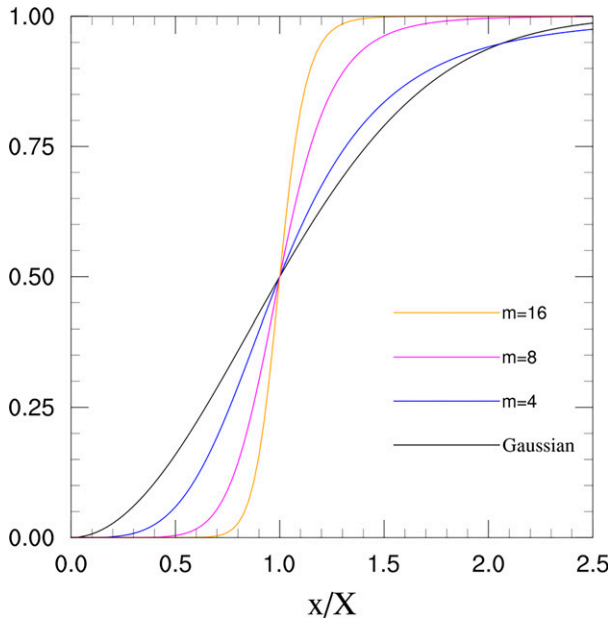
FIG. 5. Some functions that approximate the Heaviside step function $H[(x - 1)/X]$. The functions are $1 - 1/[1 + (x/X)^m]$ for $m = 4$, 8, and 16, and the complementary Gaussian function, $1 - \exp(-0.69315x^2)$.

Similarly we can visualize the effect of varying the column radius by sliding the blue line to different ordinate values while keeping the red line anchored to it. As the column radius increases, the lower limit of the integral increases and the integral decreases accordingly because the integrand is positive definite. Hence the effective buoyancy decreases at all radial distances as in Fig. 3.

A step function profile does not apply to wide high-speed cumulonimbus updrafts whose columns contain undiluted inner cores (Davies-Jones 1974) surrounded by an outer sheath where entrained exterior air has penetrated (Nowotarski et al. 2020, see their Fig. 5d). Therefore we next assume a continuous density profile.

5. Solution for a continuous radial density profile

A continuous nondimensional radial excess-density function that resembles a top-hat profile is provided by

$$\sigma_*(x) = 1 - \frac{1}{1 + (x/X)^m}, \quad m \ge 4. \tag{43}$$

Since $\sigma_*(0)$ varies from 0 at $x = 0$ to 1 at $x = \infty$ and is 0.5 at $x/X = 1$ (or equivalently $r/R = 1$), we still define R as the column radius. As m increases the profile becomes increasingly like a step function with the jump at $x = X$ (Fig. 5). For $m \ge 4$, the functions have much sharper edges than the equivalent Gaussian function $1 - \exp(-ax^2)$, $a = \ln2$, that also passes through the common point $(1, 0.5)$ of the curves (Fig. 5). The Gaussian function has the added disadvantage that it has only one parameter, a, and so cannot be steepened without narrowing the column.
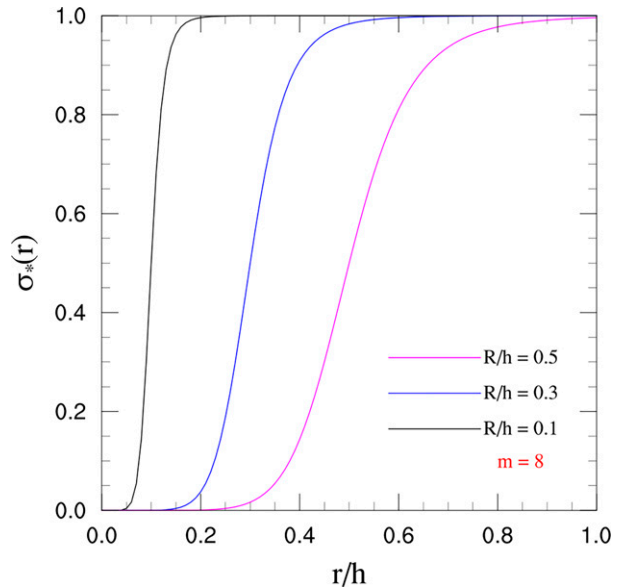

FIG. 6. Nondimensional radial density profiles as a function of r/h for $m = 8$ and $R/h = 0.1$, 0.3 and 0.5.

Figure 6 shows the nondimensional radial density profile for $m = 8$ and different column widths.

Introducing (43) into (29) produces

$$E_*(x) = -\left[1 - \frac{1}{1 + (x/X)^m}\right] + K_0(x)\int_{s=0}^{x} sI_0(s)\left[1 - \frac{1}{1 + (s/X)^m}\right]ds$$

$$+ I_0(x)\int_{s=x}^{\infty} sK_0(s)\left[1 - \frac{1}{1 + (s/X)^m}\right]ds. \tag{44}$$
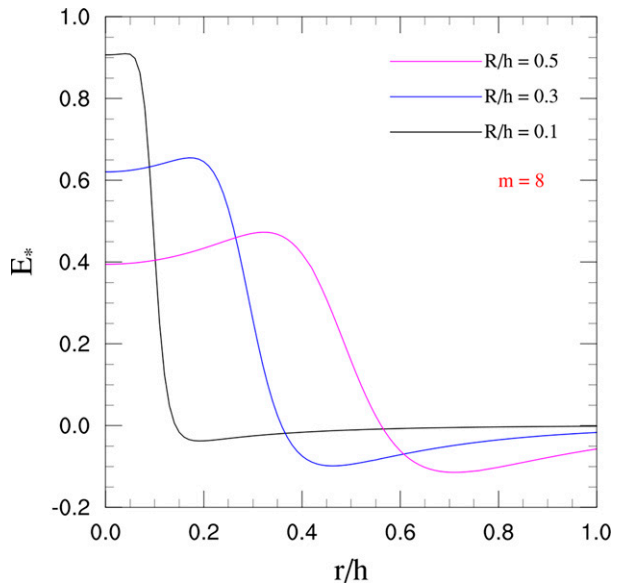

FIG. 7. Nondimensional effective-buoyancy radial profile E_* as a function of r/h for the buoyancy profiles shown in Fig. 6.
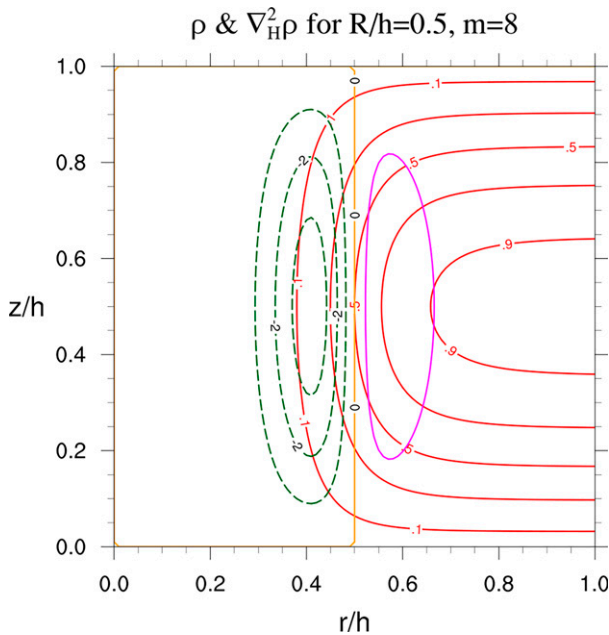
FIG. 8. The incomplete density field $[\sigma(x) - \sigma(0)]\sin\pi z/h$ (complete apart from a function of height) and the $\nabla_H^2\rho$ field. The density contours are solid red with red labels, and are in units of $g\Delta\sigma$. The contours start at 0.1 and the contour spacing is 0.2. The positive, zero, and negative contours of $\nabla_H^2\rho$ are solid magenta, solid orange, and dashed green, respectively. The contours of this field are in units of $\pi^2\Delta\sigma/h^2$ with green labels and a contour interval of 1.

This simplifies to

$$E_*(x) = \frac{1}{1 + (x/X)^m} - K_0(x)\int_{s=0}^{x} \frac{sI_0(s)}{1 + (s/X)^m} ds$$
$$- I_0(x)\int_{s=x}^{\infty} \frac{sK_0(s)}{1 + (s/X)^m} ds \qquad (45)$$

by subtracting (A20). The integrals in (45) were computed to an accuracy of 10^{-4} with code from Press et al. (1992, 130–133). The second integral was calculated with an upper limit of $x = 25$ instead of infinity.

Figure 7 shows the NEBRP as a function of r for the $m = 8$ density profile and different column widths. The NEBRP now changes sign from positive to negative just outside the nominal column edge. Essentially the curves in Fig. 7 are just smooth versions of the ones in Fig. 2. The cusps are rounded off, and the jump has become a smooth transition zone with a reduced amplitude.

The density field (minus a function of height) and its horizontal Laplacian, $\nabla_H^2\rho$, are shown in Fig. 8 for a nominal column radius R of 0.5 h and $m = 8$. From (9), $\nabla_H^2\rho$ is the forcing function for effective buoyancy β. For the positive radial density gradient depicted, $\nabla_H^2\rho$ is positive in an annular region just inside and negative outside $r = R$. This pattern associates with positive β just inside and negative β outside $r = R$ as shown in Fig. 9.

6. Summary

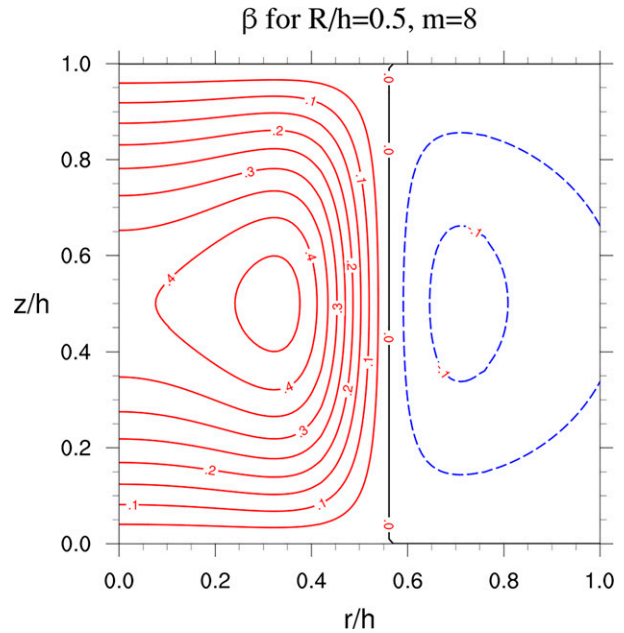We assume axisymmetric density distributions in a domain that extends radially to infinity and, using the DJ03 theory,

FIG. 9. Effective buoyancy field β. The positive, zero, and negative contours of β are solid red, solid black, and dashed blue, respectively. The β contours are in units of $g\Delta\sigma$ with a contour interval of 0.05.

find solutions for the associated effective buoyancy per unit volume. As proven by DJ03, the effective buoyancy *per unit volume* is totally independent of the choice of a basic-state density. For radial density profiles (11) that are step functions, (36) provides analytical solutions for effective buoyancy. These solutions qualitatively replicate in axisymmetric geometry several features of SM22's 2D numerical solution. For continuous density profiles (43) that approximate (11), the solutions (44) are just smooth versions of the corresponding ones (36) for discontinuous density profiles.

The negative effective buoyancy at the column edge in SM22's numerical solutions and the analytical solutions herein are consistent with data obtained by jet aircraft flying through severe storms. These data reveal a descending sheath of air surrounding the updraft core (Sinclair 1973).

APPENDIX

Properties of Modified Bessel Functions

The following useful formulas involving modified Bessel functions are listed here for reference in the main text. In

the domain $[0, \infty)$, $I_0(x)$ and $I_1(x)$ are monotonically increasing functions with

$$I_0(0) = 1, \quad I_1(0) = 0, \quad I_0(\infty) = I_1(\infty) = \infty, \quad \text{(A1)}$$

and $K_0(x)$ and $K_1(x)$ are monotonically decreasing functions with

$$K_0(0) = K_1(0) = \infty \quad K_0(\infty) = K_1(\infty) = 0. \quad \text{(A2)}$$

The properties of these modified Bessel functions are (Jeffrey 1995)

$$\frac{dI_0(x)}{dx} = I_1(x), \quad \text{(A3)}$$

$$\frac{dK_0(x)}{dx} = -K_1(x), \quad \text{(A4)}$$

$$\frac{d[xI_1(x)]}{dx} = xI_0(x), \quad \text{(A5)}$$

$$\frac{d[xK_1(x)]}{dx} = -xK_0(x), \quad \text{(A6)}$$

$$\int_{s=0}^{x} sI_0(s)ds = xI_1(x), \quad \text{(A7)}$$

$$\int_{s=x}^{\infty} sK_0(s)ds = xK_1(x), \quad \text{(A8)}$$

$$I_0(x) \to 1 \quad \text{as } x \to 0, \quad \text{(A9)}$$

$$I_1(x) \to \frac{x}{2} \quad \text{as } x \to 0, \quad \text{(A10)}$$

$$K_0(x) \to -\ln(x/2) \quad \text{as } x \to 0, \quad \text{(A11)}$$

$$xK_1(x) \to 1 \quad \text{as } x \to 0, \quad \text{(A12)}$$

$$I_n(x) \to \frac{e^x}{\sqrt{2\pi x}} \quad \text{as } x \to \infty \quad \text{for } n = 0, 1, \dots, \quad \text{(A13)}$$

$$K_n(x) \to \sqrt{\frac{\pi}{2x}} e^{-x} \to 0 \quad \text{as } x \to \infty \quad \text{for } n = 0, 1, \dots. \quad \text{(A14)}$$

According to L'Hôpital's rule,

$$x \ln x \to -x \quad \text{as } x \to 0, \quad \text{(A15)}$$

$$\therefore xK_0(x) \to 0 \quad \text{as } x \to 0. \quad \text{(A16)}$$

The Wronskian $W(x)$ of $I_0(x)$ and $K_0(x)$, is defined by

$$W(x) \equiv I_0(x) \frac{dK_0(x)}{dx} - \frac{dI_0(x)}{dx} K_0(x). \quad \text{(A17)}$$

Inserting (A3) and (A4) produces

$$W(x) = -I_0(x)K_1(x) - I_1(x)K_0(x). \quad \text{(A18)}$$

By Abel's formula in Hildebrand (1965, p. 230) applied to the modified Bessel equation or by formula (9.6.15) in Abramowitz and Stegun (1964, p. 375),

$$W(x) = -1/x, \quad \text{(A19)}$$

$$\therefore \ 0 = -1 + xI_0(x)K_1(x) + xI_1(x)K_0(x). \quad \text{(A20)}$$

Introducing (A7) and (A8) into (A20) results in

$$0 = -1 + I_0(x) \int_{s=x}^{\infty} sK_0(s)ds + K_0(x) \int_{s=0}^{x} sI_0(s)ds. \quad \text{(A21)}$$

REFERENCES

Abramowitz, M., and I. A. Stegun, 1964: *Handbook of Mathematical Functions with Formulas, Graphs, and Mathematical Tables*. U.S. National Bureau of Standards, 1046 pp.

Davies-Jones, R. P., 1974: Discussion of measurements inside high-speed thunderstorm updrafts. *J. Appl. Meteor.*, **13**, 710–717, https://doi.org/10.1175/1520-0450(1974)013<0710:DOMIHS>2.0.CO;2.

——, 2002: Linear and nonlinear propagation of supercell storms. *J. Atmos. Sci.*, **59**, 3178–3205, https://doi.org/10.1175/1520-0469(2003)059<3178:LANPOS>2.0.CO;2.

——, 2003: An expression for effective buoyancy in surroundings with horizontal density gradients. *J. Atmos. Sci.*, **60**, 2922–2925, https://doi.org/10.1175/1520-0469(2003)060<2922:AEFEBI>2.0.CO;2.

Doswell, C. A., III, and P. M. Markowski, 2004: Is buoyancy a relative quantity? *Mon. Wea. Rev.*, **132**, 853–863, https://doi.org/10.1175/1520-0493(2004)132<0853:IBARQ>2.0.CO;2.

Emanuel, K. A., 1994: *Atmospheric Convection*. Oxford University Press, 580 pp.

Glickman, T. S., Ed., 2000: *Glossary of Meteorology*. 2nd ed. Amer. Meteor. Soc., 855 pp.

Hildebrand, F. B., 1965: *Methods of Applied Mathematics*. 2nd ed. Prentice-Hall, 362 pp.

Jeevanjee, N., and D. M. Romps, 2015: Effective buoyancy, inertial pressure, and the mechanical generation of boundary layer mass flux by cold pools. *J. Atmos. Sci.*, **72**, 3199–3213, https://doi.org/10.1175/JAS-D-14-0349.1.

——, and ——, 2016: Effective buoyancy at the surface and aloft. *Quart. J. Roy. Meteor. Soc.*, **142**, 811–820, https://doi.org/10.1002/qj.2683.

Jeffrey, A., 1995: *Handbook of Mathematical Formulas and Integrals*. Elsevier, 410 pp.

Morrison, H., 2017: An analytic description of the structure and evolution of growing deep cumulus updrafts. *J. Atmos. Sci.*, **74**, 809–834, https://doi.org/10.1175/JAS-D-16-0234.1.

Nowotarski, C. J., J. M. Peters, and J. P. Mulholland, 2020: Evaluating the effective inflow layer of simulated supercell updrafts. *Mon. Wea. Rev.*, **148**, 3507–3532, https://doi.org/10.1175/MWR-D-20-0013.1.

Pauluis, O., and S. Garner, 2006: Sensitivity of radiative–convective equilibrium simulations to horizontal resolution. *J. Atmos. Sci.*, **63**, 1910–1923, https://doi.org/10.1175/JAS3705.1.

Press, W. H., S. A. Teukolsky, W. T. Vetterling, and B. P. Flannery, 1992: *Numerical Recipes in Fortran 77*. 2nd ed. Cambridge University Press, 1010 pp.

Rotunno, R., and J. B. Klemp, 1982: The influence of the shear-induced pressure gradient on thunderstorm motion. *Mon. Wea. Rev.*, **110**, 136–151, https://doi.org/10.1175/1520-0493(1982)110<0136:TIOTSI>2.0.CO;2.

Saltzman, B., 1962: *Selected Papers on the Theory of Atmospheric Convection with Special Application to the Earth's Planetary Atmosphere.* Dover, 461 pp.

Sinclair, P. C., 1973: Severe storm air velocity and temperature structure deduced from penetrating aircraft. Preprints, *Eighth Conf. on Severe Local Storms*, Denver, CO, Amer. Meteor. Soc., 25–32.

Smith, R. K., and M. T. Montgomery, 2022: Effective buoyancy and CAPE: Some implications for tropical cyclones. *Quart. J. Roy. Meteor. Soc.*, **148**, 2118–2131, https://doi.org/10.1002/qj.4294.

Tarshish, N., N. Jeevanjee, and D. Lecoanet, 2018: Buoyant motion of a turbulent thermal. *J. Atmos. Sci.*, **75**, 3233–3244, https://doi.org/10.1175/JAS-D-17-0371.1.